Wind-generated water waves in a wind tunnel: Free surface statistics, wind friction and mean air flow properties

Sandro Longo

Department of Civil Engineering, University of Parma, Parco Area delle Scienze, 181/A, 43100 Parma, Italy

ARTICLE INFO

ABSTRACT

This paper describes the systematic measurements of wind and water waves in a wind tunnel with a water tank inside. The velocity fields are measured using a 2-D Laser Doppler velocimetry (LDV) in air and the instantaneous water levels are measured using resistive twin-wire probes. The paper gives details on the free surface statistics and the mean airflow structures, including the statistics of the wind-generated water waves, phase velocity and group velocity of the waves, waves grouping, and interface friction. Comparisons are made between these results with those for wind flows over a fixed solid surface. The wind-generated waves show the typical growing trend with fetch and wind speed and are also asymmetric, with crests more pronounced than troughs. A model is developed to account for the relative variation of phase velocity and group velocity, which includes a dependence of the drift velocity from the wave steepness. The statistics of the wave groups suggest that a separate treatment of the envelopes of the crests and of the troughs should be necessary. The air flow boundary layer over the water waves shows a logarithmic profile with a wake near the free stream and the apparent roughness is related to the wave amplitude. The transition to turbulence occurs at an earlier stage with respect to the transition of a boundary layer over a smooth, flat rigid wall. The thickness of the boundary layer over the water waves grows much faster than for the boundary layer over a plain, smooth solid wall.

© 2011 Elsevier B.V. All rights reserved.

1. Introduction

In recent decades, many studies on airflow and water interactions have been published, and numerous models have been developed to understand and predict the dynamics of the flows and wave generation mechanisms. The air–sea interface covers more than 70% of the Earth's surface and low-speed winds transfer the momentum to water, generating waves, currents and turbulence. The wind wave generation regime with currents and surface drift is less frequently studied than the pure ocean waves. Considering only the wave generation, the fundamental works by Phillips (1957) and Miles (1957) gave a general framework for the free surface disturbances excited by pressure fluctuations and followed by the growth mechanism, with the feedback from the perturbations of the air-flow to the free surface waves. However, this framework lacks experimental support. Because the measured growth rate was much larger than the theoretical predictions, other models were developed by Longuet-Higgins (1969), who showed that an oscillating shear stress could be as effective as the wave-induced pressure in transferring energy from wind to waves. It soon became necessary to develop turbulent models instead of quasi-laminar models. The problem in developing turbulent

models is the generality: the available results are often inconsistent and restricted to specific conditions; hence, it is difficult to establish a generic model. A model that is calibrated in different flow conditions cannot be transferred to other flow situations. Also, the reference system can be fixed or wave-following, with strong differences in the results and in the interpretation. The wave generation is affected by the turbulence not only on the air side, but also on the water side, as analysed by Teixeira and Belcher (2006). The process is complex, and despite numerous improvements in the analysis of the detailed mechanisms involved, details are still unknown. A general description of the interactions between turbulence and an air–water interface is reported in Brocchini and Peregrine (2001) while the coupling processes between gravity waves and winds and currents in turbulent boundary layer are widely discussed in Sullivan and McWilliams (2010).

Apart from the momentum transfer in wave and current generation, the air–water exchange of gases also has environmental implications and is a critical factor in understanding the fate of pollutants or other anthropogenic materials. Global budgets of various materials have been computed based on parametric models, but the exchange process at the air–water interface is poorly understood. Turbulence as well as the surface tension is important in determining the gas-transfer rate through the interface, but their contributions have different orders of magnitude: a small drop of a surfactant can reduce the gas-transfer rate by up to 60% without affecting the turbulence structure (McKenna, 2000). Therefore, most of the process occurs in

E-mail address: sandro.longo@unipr.it.

a thin layer in which the turbulence itself is suppressed and molecular motion is dominant.

On the water side, the structure of the flow field beneath the interface depends on the wind speed and the fetch. In the lab, for a fixed wind speed in the first zone just downstream, there are tiny undulations at the air–water junction; in the second zone, the waves grow, with rounded crests and sharp troughs. Caulliez et al. (1998) reported that these growing waves occur in the form of V-shaped streaks, which are randomly distributed and are generally unstable. At a small wind velocity, before the onset of surface waves, a shear-driven current develops. A mixed typical wave motion is superimposed at a higher wind speed. At this stage, the convective motion is still limited, and the turbulence is transferred from the mean flow by shearing and micro-breaking. Micro-breaking differs from the classical wave breaking because it occurs in short waves without entraining air. On the ocean scale, micro-breaking occurs more frequently than the classical wave breaking, and it is believed to be important in transferring chemicals and gases (Banner and Peregrine, 1993). In the lab, the percentage of micro-breaking increases dramatically from ~10% to ~80% as the wind speed increases from ~5 m/s to ~7 m/s and reaches ~90% for wind speeds larger than ~11 m/s (Siddiqui and Loewen, 2007).

Most of the experimental and theoretical activities have clarified the overall behaviour of the system, yet several specific phenomena have not been well described, and their effects are interconnected. The air–water interface separates the two boundary layers: the airflow boundary layer and the water flow boundary layer. They share many characteristics with the boundary layers generated by a rigid surface, but they have additional characteristics due to their interactions. Some researchers have attempted to study the airflow by mimicking the water waves with a rigid undulated wall, but the similarity fails in reproducing some important phenomena due to the lack of wave breaking and wave mixing processes (see Perry et al, 1987, for turbulent structure in boundary layers above wavy rigid surfaces). Other models, especially for the boundary layer on the water side, assume that the interface is flat (e.g. Shen and Yue, 2001). Clearly wave breaking and Langmuir circulation increase the turbulence level, which cannot be reproduced by a flat surface. Langmuir circulation and wind wave generation can occur over comparable time scales (Melville et al., 1998), and both act as turbulence sources. As a consequence, diffusion is much larger on the water side boundary layer in the presence of water waves (Veron and Melville, 2002). In the presence of interface waves, the local balance of turbulent quantities in the boundary layer involves the transport from the sea surface as well as production and dissipation; while for the case of rigid wall turbulence, production simply equals to dissipation. Researchers previously analysed the mean airflow profile and compared the similarities and differences between the profiles over the smooth and rough plate (Hsu et al., 1981; Stewart, 1970). Gerbi (2008), who analysed the mechanisms of turbulent diffusion, posed several questions regarding the differences between the rigid plate boundary layer and the water boundary layer with an air/water interface.

The flow field is characterised by different geometric scales, and a variety of structures can simultaneously develop. The scales involved in the two boundary layers range from millimetres to tens of metres (in the field). Clearly, turbulence plays a major role, and all of the fluxes (momentum, chemicals, gas) are strongly controlled by coherent structures, which are almost always present in the flow fields. Siddiqui et al., 2004, investigated the property of the near surface flow, and by correlating the gas-transfer rate with the surface renewal, they found that 60% of the gas-transfer rate was due to coherent structures. This result suggests that proper attention should be given to the effects and efficiency of coherent structures.

Unfortunately, most quantities related to turbulence are difficult to measure in the field due to the presence of surface gravity waves that have much larger fluctuations than those of turbulence. The problem of fluctuation separation has been addressed in several

ways. Kitaigorodskii et al. (1983) separated the velocity signal according to the free surface displacement, while Trowbridge (1998) and Shaw and Trowbridge (2001) distinguished turbulence from waves using the expected variations of waves. Then, the fluxes and the length scale near the bed were evaluated. Cavaleri and Zecchetto (1987) attempted to estimate the momentum flux near the free surface and found that the results were strongly affected by the separation method.

Wind friction is the most used and probably the optimal indicator of efficiency in transferring momentum and several other quantities between air and water. On a global scale, the budgets of energy strongly depend on this single coefficient which, in turn, should be evaluated with the best possible accuracy. On a local scale, wind growth, wave breaking, meteorological tides are phenomena strictly controlled by the wind friction. Nevertheless there are still some information missing on the relationship between free stream wind velocity and friction at the interface in non-stationary conditions (e.g. during wind growth) or in a physically limited domain (e.g. in bay or estuaries). Also chemical and gases exchange is expected to follow a similar mechanism of the momentum transfer and hence to depend also on wind friction.

The necessity to analyse further details of the phenomena is also confirmed by numerous papers which continuously appear on this topic. Amongst them the most recent are due to Liberzon and Shemer (2011) and to Shaikh and Siddiqui (2011), which follow an experimental topic started several tens of years ago.

In order to clarify some aspects of the involved phenomena, a series of tests in a wind tunnel equipped with a water tank has been carried out. Gravity waves are generated entirely by the wind, and the results are analysed. This paper is organised as follows: in Section 2, the experimental apparatus and the measurements procedures are described. In Section 3, the experimental results on water waves are presented and discussed, with a focus on the phase and group velocities, and wave grouping. Then, the air flow mean characteristics are presented, with details on the vertical profile, apparent roughness and boundary layer thickness. The conclusions are presented in Section 4.

2. Experimental apparatus and procedures

The experiments were conducted in a small non-closed low-speed wind tunnel in the Centro Andaluz de Medio Ambiente, CEAMA, University of Granada, Spain. The boundary layer wind tunnel has a PMMA structure with a test section that is 3.00 m in length with a 360 mm × 430 mm cross-section. The wind velocity, up to 20 m/s, is controlled by a variable frequency converter controlling an electric fan in the downstream section with a maximum power of 2.2 kW. The air flow is straightened by a honeycomb section connected to the tunnel followed by a contraction. A water tank is installed to allow water wave generation. The water tank is constructed of PVC and is 970 mm in length and 395 mm high (internal size), while the still water depth is 105 mm. The overall layout is shown in Fig. 1. The air flow cross-section over the tank is 235 mm × 430 mm and is connected to the wind tunnel through an upstream ramp and a downstream ramp. The upstream ramp avoids air flow separation and guarantees a stable thin boundary layer above the water surface. The downstream ramp is required to reduce energy loss and avoid large unsteady vortices, which can induce pulsating motions in the air stream, hence smooth air flow can be maintained. At the downstream end of the tank, the PVC side is slightly higher than the upstream side wall to limit the overtopping of generated waves, and a wave absorbing system of stainless steel wool is used to minimise reflection.

One side of the tank is constructed of glass (thickness 5 mm) to allow optical access. The details of the flow field and definition of symbols are shown in Fig. 2. Further details can be found in Chiapponi et al., 2011.
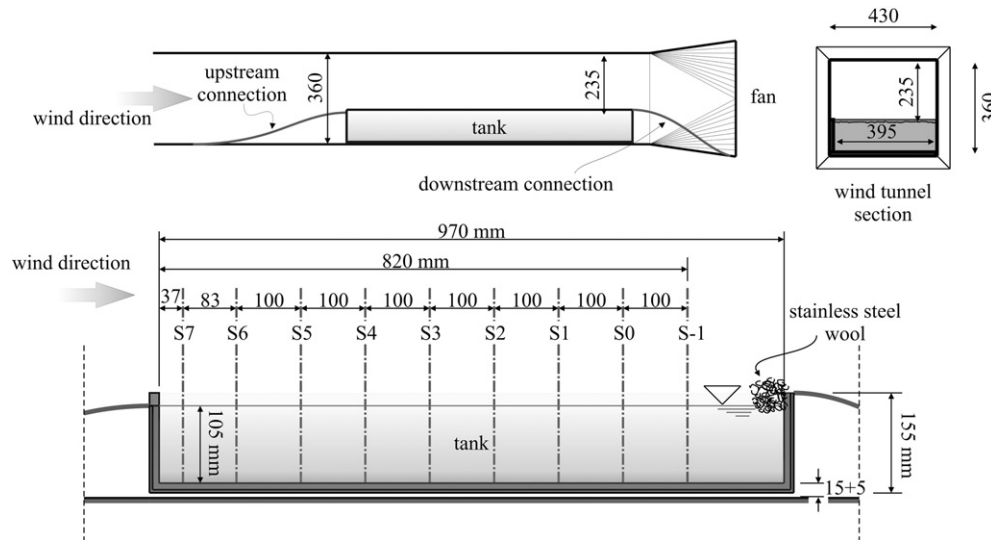
Fig. 1. Layout of the wind tunnel and water tank.

2.1. Fluid velocity measurements

The wind speed in the tunnel is measured with a TSI 2D Laser Doppler velocimetry (LDV) system. At first, the wind speed was measured by a hot-wire film connected to a TSI IFA, but this was soon dismissed because the water droplets could attach to the sensor and possibly damage the quartz coating film.

The laser source is an Innova 70 Series water-cooled Ar-Ion laser, which can reach a maximum power of 5 W and works with two pairs of laser beams with different wavelengths (green, $\lambda_g = 514.5$ nm and blue, $\lambda_b = 488.0$ nm); each pair define a plane, and the two planes are perpendicular to each other. The TSI optical modular system has a two-component fibre optics transmitting/receiving probe, which also collects the scattered light, sending it to the elaboration system, as the system works in backward scatter mode. The focus length of the probe lens is 363 mm, and the beam spacing is 50 mm. The half-angle between the incident beams is 3.96°. The measurement volume is defined by the intersection of the four laser beams, and has the shape of a prolate ellipsoid whose dimensions are ~0.08 mm × 0.08 mm × 1.25 mm.

The transmitting/receiving equipment of the LDV is mounted on an ISEL traverse system and is placed adjacent to the wind tunnel (Fig. 3). The traverse system allows longitudinal (parallel to the wind tunnel) and vertical displacements of the probe, which are controlled by a MATLAB® programme that transfers data to a Controller ISEL C142 4.1. The stepper motors of the traverse system have a resolution of 1 step = 0.0125 mm, but the overall accuracy in the probe position is expected to be equal to 0.1 mm.

The reference system for the transverse displacements and the velocity measurements has its horizontal origin ($x=0$) at the upstream end of the water tank and its vertical origin ($z=0$) at the still water level. The position of the still water level was defined at the beginning of each series of measurements, moving the probe in the vertical in order to have the intersection of the LDV beams exactly at the free surface. The signal of a correct vertical positioning was a huge increment of data rate, due to the particles of dust in random motion at the interface.

In addition to the position of the probe, its inclination with respect to the horizontal plane could be changed. A positive angle β enables the air flow measurements immediately above the water surface, and the value $\beta = +4.2°$ is fixed.

The last parameter set for the LDV velocity measurements is the orientation of the laser beams. The laser coordinate system can be rotated by an angle θ with respect to the external coordinate system made of the horizontal (x) and vertical (z) axes. For the present experiments, a rotation $\theta = 45°$ is set to reach points close to the interface. It should be noted that the LDV coordinate system 1–2 is the system with which the velocity components are actually measured, and a coordinate transformation is conducted to get the velocity components in the external system, which is possible by assuming that the flow is 2-D.

For measurements in the air, water drops generated by a spray gun are used for seeding. The spray gun is outside of the wind tunnel, with the nozzle pointed toward the honeycomb section at the entrance of the wind tunnel. This setup ensures that the large water droplets are captured by the honeycomb section and that only the
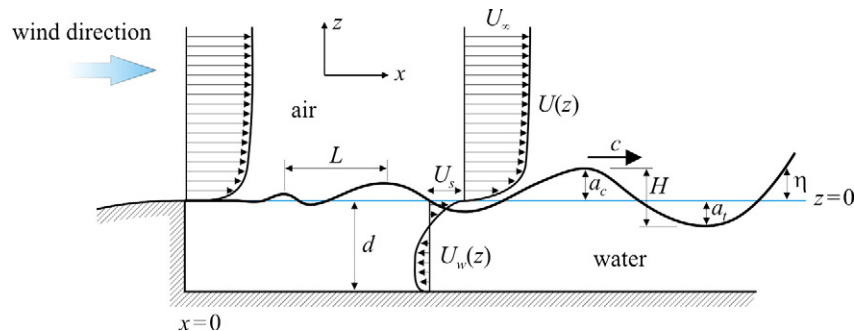

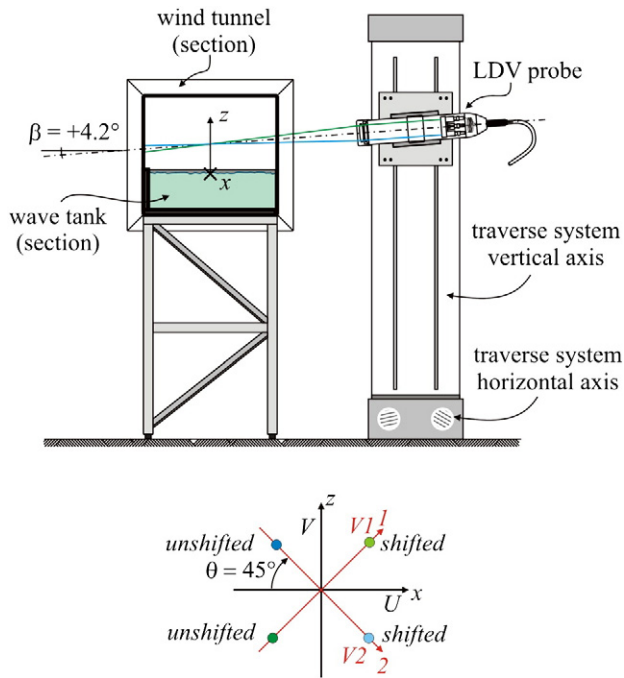**Fig. 2.** Air water motion description and symbol identification.

Fig. 3. Layout of the LDV probe and the reference systems.

2.2. Water level measurements

The water level can be measured using three different instruments: an ultrasound distance metre in the air, positioned on top of the wind tunnel; resistance probes in the sections of the measurements; and the echo output of the ultrasound Doppler velocity profiler. For the free surface data analysis in this paper (wave statistics and phase and group velocity estimation), the resistance probes are preferred. There are 8 resistance probes always connected and positioned in Sections from S7 to S0. Occasionally, an additional resistance probe in Section S-1 (the largest fetch) is connected but most of the results of the water level measurements in Section S-1 have been obtained with the ultrasound Doppler velocity profiler. The resistance probes are quite accurate but have a limitation in resolution in the order of the height of the water meniscus around the wires. Also, the cross-talking influences the measurements, and even though the probes are positioned with the two wires aligned along the expected wave crest (i.e. spanwise), the spatial resolution can be assumed to be equal to the spacing of the wires. The probes have the advantage of simultaneous measurement in several sections and hence the possibility of cross-correlation the water level elevations.

The water level measurements are performed simultaneously at all sections (S0 to S7) using 8 probes, and the data are acquired at a rate of 200 Hz through a DAQ board after filtering with a low-pass filter at 20 Hz. The hardware is produced by DHI (water level modules, filter, DAQ), but the 8-wave gauges were produced in the lab with twin parallel wires ($\phi = 0.3$ mm) at a spacing of 20 mm. The calibration is conducted by modifying the water level in the expected range and measuring the input value through an ultrasound distance metre installed in the wind tunnel over the tank. The hardware modules are set with the maximum gain and with the zero offset corresponding to an empty tank.

3. Results and discussion

3.1. Waves

The wind-generated waves and their evolution have been studied by numerous researchers (e.g., Wu, 1975) under various conditions; at low wind velocity ($U_\infty < 1.9$ m/s), capillary waves are generated, followed by rhombic gravity cells due to the wind boundary layer transition to turbulence. At higher wind velocity, wave breaking occurs, and gravity replaces the surface tension as the key parameter for the wind–wave interaction.

A similar behaviour is observed in the present experiments. Some small disturbances of the free surface have wavelengths of less than 1 cm, and the wave crests are oriented normally to the wind direction. For increasing wind speeds, the small waves become larger in amplitude and length, reducing the frequency and increasing the travelling speed. The high wind speed is responsible for the dissipative micro-breaking, while the capillary effect is very limited. In fact, micro-breaking frequently occurs in the experimental conditions for high wind speeds (Siddiqui and Loewen, 2007). The instantaneous water surface elevation data are first analysed in the time domain with a zero-up-crossing technique to extract statistical parameters. The statistical values of the wave height H, the crest a_c and the trough a_t are reported in Table 1 and sketched in Fig. 4 for the maximum and minimum wind speed tests.

The zero(-up)-crossing analysis shows a non-monotonic increase in the wave height (all statistical estimators) with wind speed and has a strong asymmetry, with the crest being more than 50% higher than the troughs. For the increasing wind speed, the free surface spectrum shows that most of the energy is stored within single peaks, with the frequency gradually reducing from ~7 to ~5 Hz. The wave growth is also linked to energy transfer towards lower frequencies due to non-linear wave-wave interactions. Note that this process is

fine droplets reach the test section. The strong effects that surfactants have on water wave generation necessitate the regular cleaning of the wind tunnel and the water tank. The LDV system measures the velocity of the particles and not of the fluid; however, small light particles follow the fluid motion well, as indicated by many studies.

The uncertainties in the LDV systems arise from velocity bias, the inhomogeneous distribution of tracer particles, errors in the individual velocity measurements, velocity gradients in the measurement volume, errors in the optical system, low resolution of the detector and the signal processing. These sources may be viewed as different types of noise that represent the white noise from stray light (reflections or scattering of laser light from walls, windows or optical components), the photomultiplier and the associated electronics. A weighting function based on the transit time was applied to correct the velocity bias due to the dependence of the sampling on the velocity magnitude. The overall uncertainty is equal to ~1% of the estimated velocity. The measurements last for 600 s except for some tests with data overflow, which limits the time of acquisition to no less than 400 s.

During the tests, the mean water level is reduced due to evaporation and overtopping of the generated waves. To control the mean water level, the tank is connected to a piezometer through a plastic tube to avoid the water-level fluctuations. An ultrasound distance metre measures the water level in a piezometer connected to the water tank. The operator periodically reads the water level in the piezometer as detected by the ultrasound distance metre and fills up the wave tank through the tube if the variation is greater than 0.2 mm. The accuracy of the mean water level position is expected to be within 0.3 mm.

After turning on the wind tunnel fan, it is necessary to wait long enough for the air stream and for the water level control system to reach a stationary state. In fact, immediately after the start of the fan, a pressure reduction on the free surface of the wave tank is responsible for a reduction of the water level in the piezometer. This variation is always less than 10 mm, equivalent to ~1 mbar, and accordingly, a tiny mass flux from the piezometer tank towards the wave tank is generated. The effect is simply due to the pressure gradient (with respect to the atmospheric pressure) generated by the initiation of the fan.

Table 1

Statistics of the waves generated by the maximum wind speed test ($U_\infty = 10.90$ m/s): wave height, crest and trough amplitude. H_{rms}, $a_{c\text{-}rms}$, and $a_{t\text{-}rms}$ are the root mean square values of the wave height, of the crest and of the troughs, H_{ave} is the mean wave, $H_{1/3}$, $H_{1/10}$, and $H_{1/20}$ are the one-third, one-tenth and one-twentieth wave heights, and H_{max} is the maximum wave height.

Section	x	N_{waves}	H_{rms}	$a_{c\text{-}rms}$	$a_{t\text{-}rms}$	H_{ave}	$H_{1/3}$	$H_{1/10}$	$H_{1/20}$	H_{max}
#	(mm)	#	(mm)	(mm)	(mm)	(mm)	(mm)	(mm)	(mm)	(mm)
S7	37	13,996	2.00	1.31	1.13	1.66	2.97	4.04	4.51	7.63
S6	120	8304	3.93	2.26	2.11	3.28	5.82	7.81	8.67	13.21
S5	220	6523	6.02	3.44	3.06	4.97	9.01	11.89	13.07	18.41
S4	320	6965	6.20	3.56	3.21	5.06	9.27	12.46	13.83	19.22
S3	420	6398	5.73	3.30	2.99	4.77	8.49	11.32	12.53	17.84
S2	520	6895	5.46	3.17	2.90	4.52	8.10	10.93	12.20	18.18
S1	620	7399	5.41	3.18	2.89	4.44	8.01	11.08	12.49	17.60
S0	720	6916	5.64	3.29	3.00	4.62	8.40	11.52	12.83	19.65

not monotonic: as micro-breaking initiates, part of the energy is lost, and a reduction of H_{rms} is detected. The waves are asymmetric, with crests more pronounced than troughs. The highest value of the root mean square (rms) wave height is reached in Section S4 and is then followed by a progressive reduction, and the growth trend is observed again in the last section of the measurements. At lower wind speeds, the behaviour seems similar, but the second phase (wave height reduction) is absent, at least for the limited fetch of the experiments.

At high wind speeds, a rapid growth of the waves and then a progressive reduction of the wave frequency are observed (Fig. 5).

The statistics of the wave frequency in the time domain are reported in Table 2, while the power spectrum of the free surface elevation is shown in Fig. 6. The spectra are computed with a Welch's averaged, modified periodogram spectral estimation method, using a Gaussian window with 50% overlap, resulting in 30 degrees of freedom and a spectral resolution of 0.025 Hz.

A similar analysis was performed by Liberzon and Shemer (2011) who calculated the coherence between the signals of two subsequent probes detecting the frequency of the correlated waves and the phase lag. Their results are similar to the present results, but the absolute values can be hardly compared because they define a dominant frequency of the waves based on the first order momentum of the spectrum whereas the peak frequency herein used is based on a direct observation of the spectrum shape.
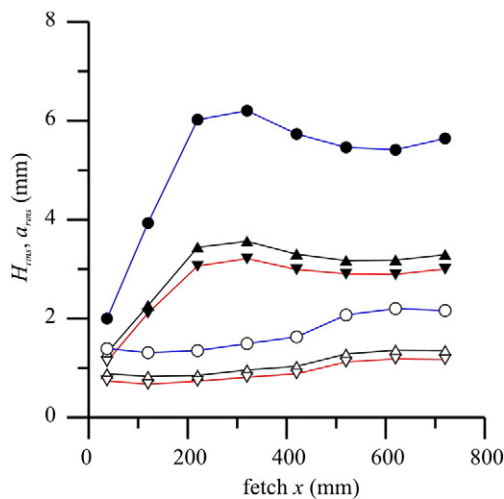
3.1.1. Phase and group velocities of the waves

In the absence of currents, the phase velocity and the wave length can be computed using the gravity-capillary wave dispersion equation:

$$\omega^2 = \left(gk + \frac{\sigma}{\rho} k^3 \right) \tanh kh \tag{1}$$

where $\omega = 2\pi/T$ is the angular frequency, T is the wave period, $k = 2\pi/L$ is the wave number, L is the wave length, ρ is the water mass density and σ is the surface tension. In the present experiments, only deep water waves are encountered, hence $\tanh kh = 1$; in addition, the waves are not rigorously monochromatic, so the values only refer to the dominant wave component.

With currents in the same direction as that of the wave propagation, the phase velocity of the wind-generated waves is greater than that indicated by the classical relationship. Minor discrepancies can also arise from the inertial pressure and finite amplitude effects. If the current has a uniform velocity across the water depth, the difference is equal to the surface drift; otherwise, the difference is less than the surface drift and depends on the velocity distribution of the current. Notably, the variation of the phase velocity due to the surface drift has been used to evaluate indirectly the wind speed (Jacobs and Gwinn, 1999).

The water level elevation measurements with the resistive probes in the 8 sections are simultaneous, therefore the cross-correlation technique is applicable for estimating the phase velocity. The average phase velocity between the two sections can be computed from the time delay τ of the highest positive peak of the cross-correlation function (Fig. 7):

$$c_{ave} = \frac{\Delta x}{\tau \pm nT} \tag{2}$$

Fig. 4. Wave height H (●), wave crest a_c (▲) and wave trough a_t (▼); root mean square values at different fetches. Solid symbols refer to the maximum wind speed ($U_\infty = 10.90$ m/s), and open symbols refer to the minimum wind speed ($U_\infty = 7.59$ m/s).
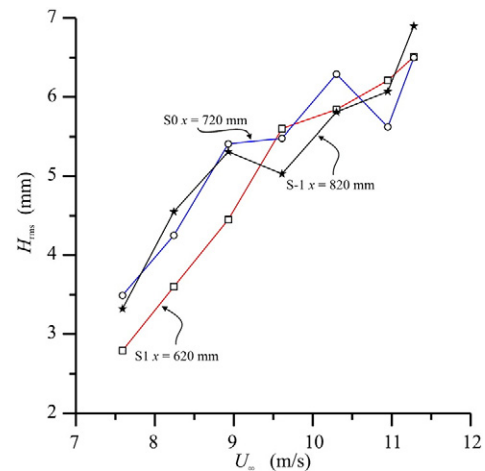
Fig. 5. Wave height growth for varying fetch and wind speed.

Table 2
Statistics of the waves generated by the maximum wind speed test ($U_\infty = 10.90$ m/s): frequency. f_{ave} is the average frequency, $f_{1/3,1/10...}$ is the frequency of the top 1/3 wave heights, of the top 1/10 wave heights, etc., and f_{max} is the maximum frequency.

Section	x	f_{ave}	$f_{1/3}$	$f_{1/10}$	$f_{1/20}$	f_{max}
#	(mm)	(Hz)	(Hz)	(Hz)	(Hz)	(Hz)
S7	37	23.26	15.38	13.16	11.76	10.00
S6	120	13.89	8.20	6.41	6.13	5.65
S5	220	10.87	6.29	5.35	5.18	5.18
S4	320	11.63	6.45	5.13	4.93	4.29
S3	420	10.64	6.13	4.95	4.76	4.69
S2	520	11.49	6.54	5.00	4.67	4.13
S1	620	12.35	6.99	5.05	4.61	4.24
S0	720	11.49	6.37	4.67	4.41	4.26

where Δx is the distance between the two probes and n is an integer. The ambiguity on the value of n has to be solved by knowing the range of the phase velocity.

The uncertainty in the estimate of the phase velocity, computed according to the propagation of error model (Taylor, 1997) is equal to

$$\frac{dc_{ave}}{c_{ave}} = \frac{d\Delta x}{\Delta x} + \frac{d\tau}{\tau \pm nT} \tag{3}$$

where the first contribution is due the vibration of the wires and to the uncertainty in the wires' position. It can be assumed that $dx = 3$ mm, and it results that $dx/x = 3\%$. The second contribution is due to the error in locating the peak of the cross-correlation function, which is due to the noise and the spectral resolution bandwidth limitation. The peak detection error in the cross-correlation is equal to (Bendat and Piersol, 2000):

$$\sigma_\tau = \frac{0.65}{\pi B \sqrt{BT}} \left(\frac{N}{S} \right) \tag{4}$$

where B is the bandwidth, T is the duration of the acquisition, and N/S is the noise-to-signal ratio. Assuming $B = 20$ Hz (the cut-off frequency of the low-pass filter in the DAQ), $T = 600$ s and $N/S = 10^{-3}$, the result is $\sigma_\tau \approx 10^{-7}$ s and is negligible. The spectral resolution bandwidth is equal to $\Delta f = 0.048$ Hz. Hence, assuming $\tau = 0.2$ s, this results in $(d\tau/2)/\tau = (f/2) \cdot \tau = 0.5\%$. The overall uncertainty is $dc_{ave}/c_{ave} = 3.5\%$.

The cross-correlation technique detects the phase velocity of a wave signal without the necessity to know the wave period (the ambiguity on the time delay can be easily solved by knowing an approximate value of the wave period). Using this information, it is possible to define the dominant wave as that having a phase velocity computed from the
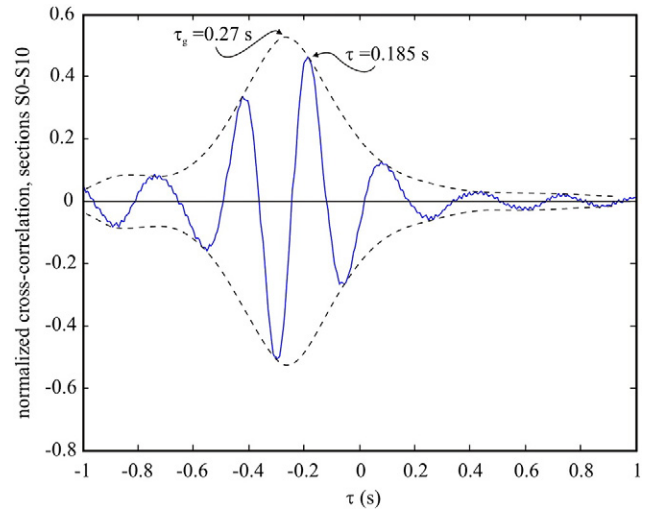

Fig. 7. Normalised cross-correlation (bold line) between the concurrent elevations in Sections S0 and S1 and the envelope (dashed line). The distance between the two probes is $\Delta x = 0.1$ m. The test with $U_\infty = 10.90$ m/s.

cross-correlation technique and a period corresponding to the peak of the energy spectrum. The spectrum is evaluated with the Welch method using a Gaussian window and 50% overlap, and the bandwidth resolution of the average spectrum is equal to 0.048 Hz. Finally, the wave length, computed as $L = c/f_p$, where f_p is the wave frequency, has an uncertainty equal to

$$\frac{dL}{L} = \frac{dc}{c} + \frac{df_p}{f_p} \approx \frac{dc}{c} + \frac{\Delta f_p/2}{f_p} \approx 4\%. \tag{5}$$

These results are reported in Table 3 for the test with the maximum wind speed. Also, the data computed for the other tests (increasing wind speed) are compared with the results of several theories and experiments in Fig. 8. In particular the empirical dispersion relation in presence of wind drift proposed by Liberzon and Shemer (2011), having the expression $c = c_0(1 + ak + bk^2)$ with $c_0 = \omega/k$ computed using the gravity capillary wave dispersion (Eq. (1)), $a = 3.05 \times 10^{-3}$ m and $b = 8.2 \times 10^{-6}$ m^2, represents an upper bound of all the data. Notably, as discussed by the authors, the two coefficients a and b are strictly related to the tank characteristics and essentially to the surface drift velocity U_s (see Section 3.2 for the analysis of the surface drift in the present paper), hence have not a general validity. The minor differences of
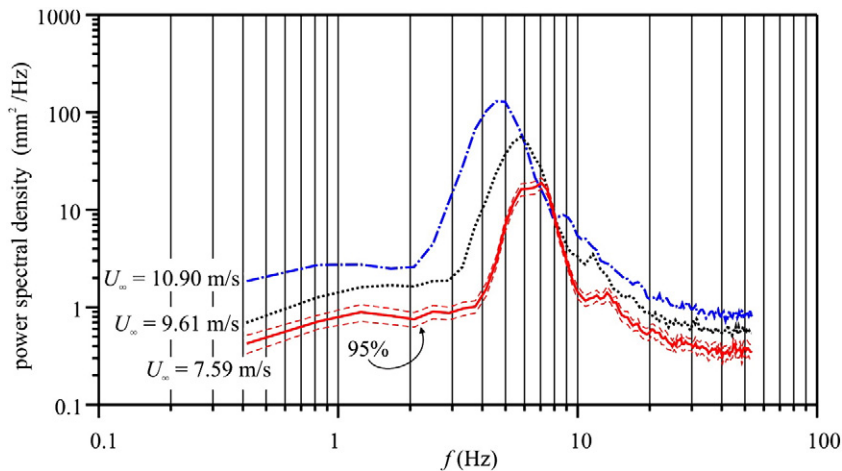

Fig. 6. Power spectrum of the free surface elevation for three tests in Section S-1 $x = 820$ mm. Measurements with the UDVP. The 95% confidence band is shown.

Table 3
Phase velocity of the waves estimated by the time delay of the peak in the cross-correlation of the water elevation signals. Values refer to $U_\infty = 10.90$ m/s. x is the fetch length, c_{ave} is the average phase celerity, f_p is the peak frequency, L is the wave length and c_{gave} is the average group celerity. Phase and group velocities are estimated as average between two close sections and the values in a section are linearly interpolated.

Section	x	c_{ave}	f_p	L	c_{gave}
#	(mm)	(m/s)	(Hz)	(m)	(m/s)
S7	37	– $0.24 \pm 3.5\%$	–	–	–
S6	120	0.30 0.35	6.20 ± 0.025	$0.048 \pm 4\%$	– $0.31 \pm 3.5\%$
S5	220	0.40 0.46	5.18	0.078	0.31 0.32
S4	320	0.48 0.51	5.27	0.092	0.36 0.41
S3	420	0.51 0.50	4.25	0.119	0.41 0.41
S2	520	0.50 0.50	3.91	0.128	0.41 0.41
S1	620	0.52 0.54	4.25	0.123	0.39 0.37
S0	720	–	3.61	–	–

the present data with respect to the theoretical dispersion relation occur for measurements near the entrance with a small fetch.

To understand the factors influencing the phase velocity, the velocity is normalised by the theoretical phase velocity for capillary-gravity waves without drift, and is plotted as a function of the relative speed of the wind and wave steepness in Fig. 9. No clear trend is observed. Presumably, the most important influencing factor is the free surface drift, which is related to the wind speed but is also dependent on the experimental tank characteristics. According to van Gastel et al. (1985), a 25% error in the surface drift U_s leads to errors in c by up to 50%.

The excess of the estimated phase velocity (proportional to the surface drift) and the estimated group velocity as a function of the wave steepness are shown in Fig. 10.
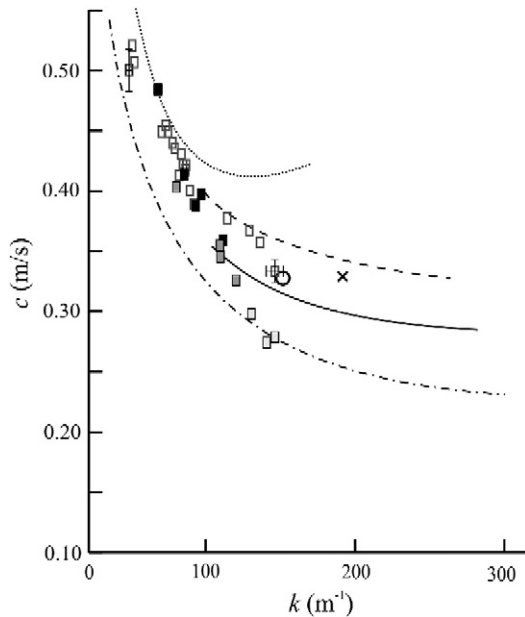

Fig. 9. Non-dimensional phase velocity c/c_0 as a function of the wave steepness kH and of the non-dimensional wind speed U_∞/c_0.

The waves are generally dispersive, thus group is different from the phase velocity. The theoretical wave group velocity is obtained by differentiating the dispersion Eq. (1), obtaining the following expression:

$$c_g \equiv \frac{\partial \omega}{\partial k} = \frac{c}{2}\left(1 + \frac{2kh}{\sinh 2kh}\right) + \frac{3}{2}\frac{\sigma}{\rho}\frac{k}{c} \to c_g = \frac{c}{2} + \frac{3}{2}\frac{\sigma}{\rho}\frac{k}{c} \text{ in deep water.} \quad (6)$$

The correction that is due to that capillarity is usually negligible unless long periods of very short waves are present.

In the present experiments, the wave group velocity is estimated by the Hilbert transform of the cross-correlation function of the measured water levels, which gives the envelope of the function with a peak at a time delay τ_g (Fig. 7). For narrow bandwidth signals, the group velocity can be computed as $c_g = \Delta x / \tau_g$ (Bendat and Piersol, 2000). The experimental results give an average value between two adjacent sections, and have an uncertainty approximately equal to the uncertainty computed for the phase velocity.

Fig. 8. Phase velocity as a function of the wave number. Theory: dashed line, Valenzuela (1976); bold line, van Gastel et al. (1985); dash-dot line, classical dispersion without drift; and dotted line, empirical relation by Liberzon and Shemer (2011). Experiments: □, present experiments, long fetch; ▪, present experiments, short fetch; ○, Plant and Wright (1980); and ×, Kawai (1979).
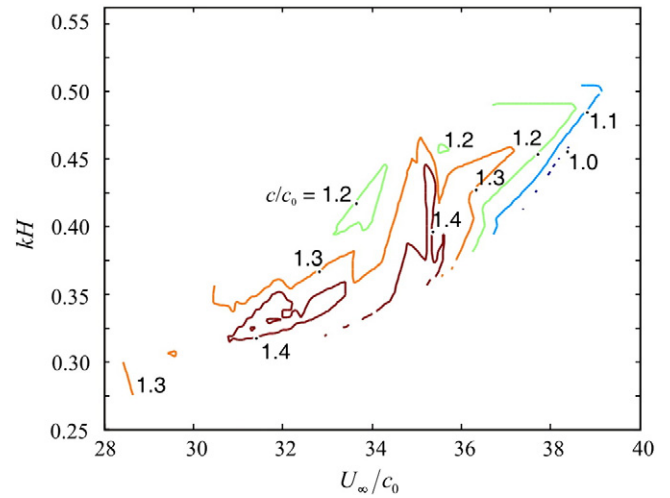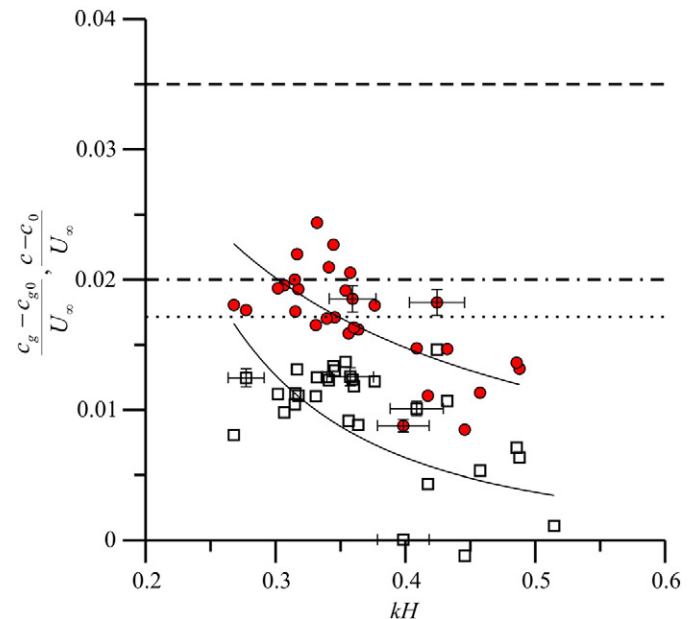

Fig. 10. Non-dimensional (□) phase velocity and (●) group velocity excess as a function of the wave steepness kH. Phase velocity excess − dashed line: Stewart (1970); dot-dashed line: Keulegan (1951) and Masch (1963); and dot line: Hidy and Plate (1966).

The excess of phase velocity and of group velocity slightly decrease with the wave steepness. The phase velocity excess respect to c_0, the velocity without currents, is smaller than the asymptotic value of $(c-c_0)/U_\infty = 0.035$ estimated by Stewart (1970) for very long fetches in the field (several kilometres). The observations by Keulegan (1951) and Masch (1963) from the technique of tracing buoyant particles indicate a value of 0.020, while those by Hidy and Plate (1966) indicate a value of 0.017. The scatter of the experimental results can be attributed to several factors, including the finite size of the buoyant particles and the velocity gradients.

The variation of the phase velocity with fetch can be attributed to several factors (wind drift and Stokes current are both variable in space), but these factors should affect the phase and the group celerities in a similar way. An attempt to explain the experimental values by assuming a dependence of the phase celerity on the wave number only is reported in Fig. 11a, where the curve is computed by using the empirical dispersion relation reported in Liberzon and Shemer (2011). Even though the trend of the curve is correct, the experimental data appear too disperse.

To explain better the experimental results, assume that the velocity drift is a function of the wave steepness $U_s = U_s(kH)$. The theoretical relationship is:

$$c \equiv \frac{\omega}{k} = \beta U_s + \sqrt{\left(\frac{g}{k} + \frac{\sigma}{\rho}k\right)\tanh kh} \rightarrow c - c_0 = \beta U_s \tag{7}$$

$$c_g \equiv \frac{\partial \omega}{\partial k} = \beta U_s + \beta kH \frac{dU_s}{dkH} + c_{g0} \rightarrow c_g - c_{g0} = \beta U_s + \beta kH \frac{dU_s}{dkH} \tag{8}$$

where β is a coefficient (Hidy and Plate, 1966). The difference between the group velocity excess respect to c_{g0}, the group velocity in absence of currents, and the phase velocity excess is due to the last term in Eq. (8).

$$\frac{c_g - c_{g0}}{c - c_0} \equiv \frac{U_s + kH \frac{dU_s}{dkH}}{U_s} = f(kH). \tag{9}$$

By assuming $f(kH) = r \cdot (kH)^\alpha$ and integrating the result is:

$$\frac{U_s}{U_{sr}} = \frac{k_r H_r}{kH} \exp\left[\frac{r}{\alpha}\left(\left(\frac{kH}{k_r H_r}\right)^\alpha - 1\right)\right] \tag{10}$$

where U_{sr} is the reference drift velocity in the section with a steepness of the waves equal to $k_r H_r$. This function has a maximum for $\frac{kH}{k_r H_r} = \left(\frac{1}{r}\right)^{1/\alpha}$ equal to

$$\left(\frac{U_s}{U_{sr}}\right)_{max} = \exp\left(\frac{1-r}{\alpha}\right) r^{1/\alpha}. \tag{11}$$

Observing the experimental $f(kH)$ in Fig. 11b two branches are evident: a first one corresponding to relevant steepness, typical of limited fetches, the second one corresponding to asymptotic wave steepness. The fitted parameters are, respectively $\alpha = -1.60$, $r = 0.62$ and $\alpha = -0.85$, $r = 0.64$.

The corresponding theoretical relative drift velocities are shown in Fig. 12.

The dashed area refers to transition between the high steepness (dashed line) and mid or low-steepness (bold line) while the dotted vertical line indicates the limit of the present tests. A similar transition is also observed in the wave height (Table 1). In the transition area the drift velocities computed by using the two experimental curves are almost coincident hence no drift velocity discontinuity is forecast. The drift velocity peaks at ~0.59 then decreases. Note that the experimental values range from ~0.57 to 1 and considering that the wave steepness almost monotonically decreases with fetch length it results that the forecast velocity drift increases from the entrance to the end of the wave tank, as expected. The comparison with some
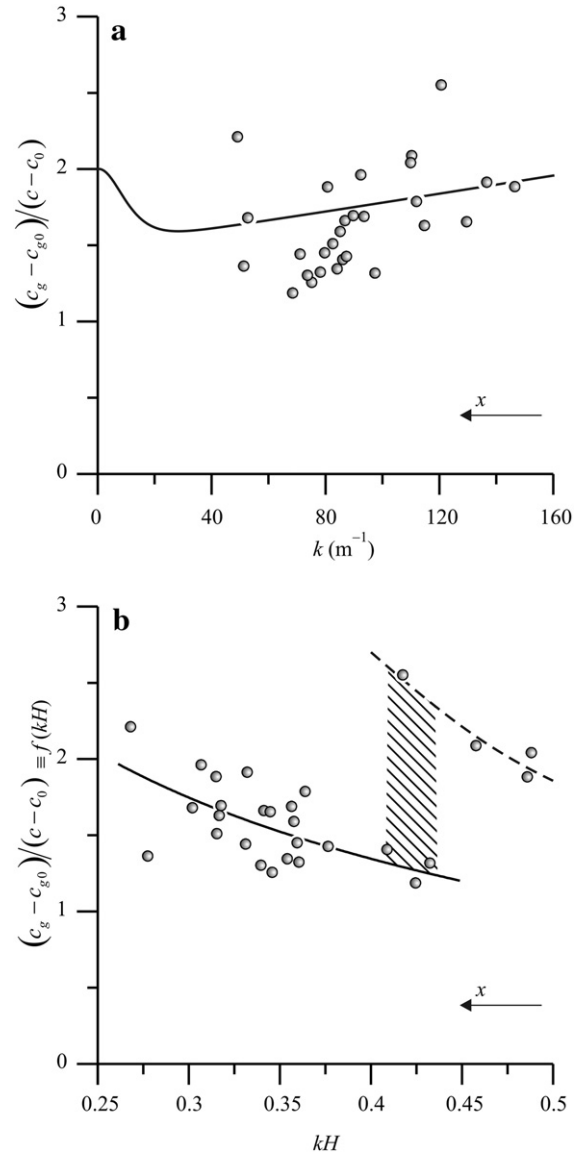

Fig. 11. a) Experimental values of the ratio between group and phase velocities as function of the wavenumber. The line is the result of the elaboration of the empirical dispersion relation by Liberzon and Shemer (2011); b) Experimental values of the ratio between group and phase velocities as function of the wave steepness. The dashed area marks a transition between high wave steepness (dashed line, $\alpha = -1.60$, $r = 0.62$), typical of wind waves in the early stage, and reduced wave steepness (bold line $\alpha = -0.85$, $r = 0.64$).

experimental data is also shown. The bullets are based on a relationship due to Wu (1975), with the wind friction velocity reported in Table 5, while the diamonds refers to few measurements obtained in the present experiments observing the horizontal velocity profile measured with LDV in water near the interface (not discussed in the present paper). Both estimations are affected by a certain degree of inaccuracy. While the empirical expression by Wu (1975) refers to developed wave field, hence no effects due to the limited size of the wave tank is accounted for, and interpolates relatively sparse data, the measurements with the LDV suffer from the strong velocity gradient in the aqueous boundary layer, which makes uncertain the correct estimation. The LDV set of measurements, even though is quite limited in number, seems to better comply with the theoretical values. Generally speaking, it is expected that the coefficient and the exponent of the function $f(kH)$ depends on the geometry of the wave field, being different for waves in open sea or in a laboratory flume.
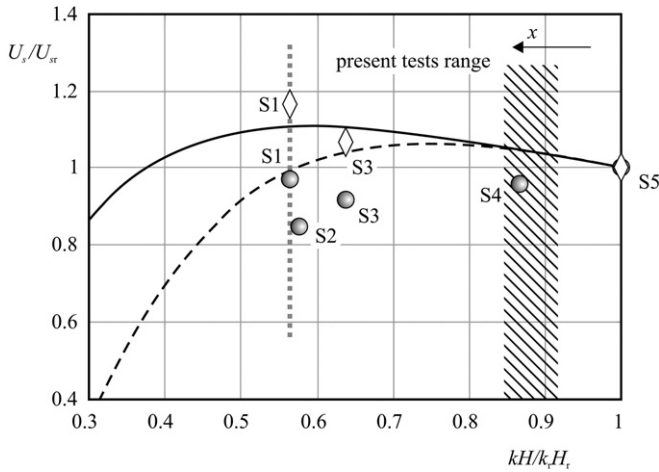
Fig. 12. Theoretical drift velocity computed according to the fitted curves in Fig. 11b. ◉: present experiments, velocity drift computed by using the relation $U_s = 0.55\, u*$ (Wu, 1975); ◇: present experiments, measured velocity drift with LDV in water (not discussed in the present paper). The dashed line refers to high wave steepness ($\alpha = -1.60$, $r = 0.62$), the bold line refers to the reduced wave steepness after transition ($\alpha = -0.85$, $r = 0.64$). The dashed area marks the transitions, the vertical dot line marks the lower limit of the wave steepness in the present experiments. The reference section is Section S5.

3.1.2. Wave grouping

A close inspection of the wave record of the real sea indicates that high waves appear in groups rather than individually. The main interest in checking for grouping in the waves generated in the tank is a closer analysis of the statistics of the free surface elevation. As explained in the following, the grouping introduces new time and length scales that can be important for further analysis of the possible resonances between the air flow field and water waves. Starting from the zero-cross analysis, the length of a group, hereafter called a *run*, is the number of consecutive waves exceeding a threshold value (see the inset in Fig. 13). The repetition length, hereafter called the *total run*, is the number of waves between two starting waves of subsequent groups (see the inset in Fig. 13). The new time and length scales are related to the length of the run (which can easily be transformed in the period of the run and length of the group) and to the length of total run (also transformable into a period and space length). The larger the threshold value, the lower the number of groups of a specific run. Following Goda (2000), the probability distribution of run length for uncorrelated waves is

$$P(j_1) = p_0^{j_1-1}(1-p_0) \tag{12}$$

where j_1 is the length of the run and p_0 is the occurrence probability for $H > H_t$, where H_t is the threshold. Real waves are correlated, and the previous hypothesis underestimates the grouping. Hence, p_{22} is defined as the probability that H_2 exceeds H_t under the condition that the previous wave H_1 has already exceeded H_t, and the probability distribution of run length for the correlated waves is

$$P(j_1) = p_{22}^{j_1-1}(1-p_{22}). \tag{13}$$

The observed probabilities are in good agreement with the theory for correlated waves, as shown in Fig. 13, where groups of up to 14 waves are present if the threshold is the median wave height. Similar results are obtained for all of the tests and all of the sections measured, with minor changes in sections with small fetches and small wind speeds. Considering that the correlation hypothesis is more realistic and gives better results, the analysis will be focussed only on the correlated wave heights.
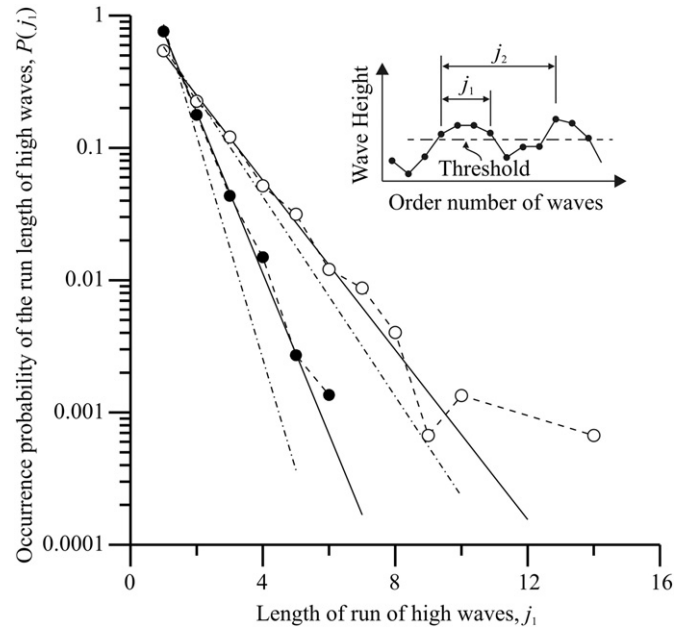

Fig. 13. Distribution of the lengths of runs of high waves exceeding the median H_{med} and $H_{1/3}$. $H \geq H_{med}$: – ○ – observations; – theory (correlated); –·– theory (uncorrelated) $H \geq H_{1/3}$: – ● – observations; Section S0, $U_\infty = 10.90$ m/s. Total of 6809 waves. $p_0(H_t = H_{1/3}) = 0.144$, $p_{22}(H_t = H_{1/3}) = 0.246$; $p_0(H_t = H_{med}) = 0.419$, $p_{22}(H_t = H_{med}) = 0.478$.

For the correlated wave heights, the mean length of the run is equal to

$$\overline{j_1} = \frac{1}{1-p_{22}} \tag{14}$$

and the mean length of the total run is

$$\overline{j_2} = \frac{1}{1-p_{11}} + \frac{1}{1-p_{22}} \tag{15}$$

where p_{11} is the probability that H_2 does not exceed H_t under the condition that the previous wave H_1 had not exceeded H_t.

A theory to evaluate the run length was developed by Kimura (1980) based on the calculations of the envelope of the waves and following the paper by Rice (1944, 1945) on the statistical properties of random noise. Assuming that the wave process is Markovian, i.e., a sequence of random states (the possible values of the wave height) having a probability distribution function (p.d.f.) that depends only on the most recent state, the probability of two successive amplitudes of the envelope R_1 and R_2 evaluated with a time lag τ is:

$$p(R_1, R_2, \tau) = \frac{R_1 R_2}{m_0^2(1-r_\tau^2)} \exp\left[-\frac{R_1^2 + R_2^2}{2m_0(1-r_\tau^2)}\right] I_0\left(\frac{r_\tau R_1 R_2}{m_0(1-r_\tau^2)}\right) \tag{16}$$

where m_0 is the zeroth order momentum, I_0 is the Bessel function of the first kind of zeroth order, and r_τ is a function of the time lag called the *envelope correlation parameter*.

The correlation coefficient computed by using the p.d.f. (16) is

$$r(R_1, R_2) = \frac{E(r_\tau) - \left(1-r_\tau^2\right)K(r_\tau)/2 - \pi/4}{1-\pi/4} \tag{17}$$

where K and E are the complete elliptic integrals of the first and second types, respectively, and r_τ is evaluated by setting the time lag τ equal to the mean wave period $\overline{T}$.

If the spectrum is narrow-banded, the function r_τ can be computed as

$$r_\tau^2 = \left| \frac{1}{m_0} \int_0^\infty S(f) \cos(2\pi f \tau) df \right|^2 + \left| \frac{1}{m_0} \int_0^\infty S(f) \sin(2\pi f \tau) df \right|^2 \qquad (18)$$

where $S(f)$ is the wave spectrum. The joint probability density function of the two successive wave heights H_1 and H_2 is

$$p(H_1, H_2, \tau) = \frac{4H_1 H_2}{H_{rms}^4 (1 - r_\tau^2)} \exp\left[-\frac{H_1^2 + H_2^2}{H_{rms}^2 (1 - r_\tau^2)} \right] I_0 \left(\frac{2r_\tau H_1 H_2}{H_{rms}^2 (1 - r_\tau^2)} \right) \qquad (19)$$

and the correlation coefficient between the two successive wave height is equal to $r(R_1, R_2)$.

The comparison between this theory and the results of the present experiments are shown in Fig. 14. The wave height correlation coefficient measured in the present tests is smaller than the theoretical prediction, i.e., for a given envelope correlation parameter, the successive wave heights correlate less than expected. It can be attributed to several reasons. First of all, the wave spectrum recorded in the sections of measurements is not actually narrow banded, because the wave generation process is dominant with respect to the wave-wave non-linear interaction, and therefore, a great variety of waves are still present. Secondly, there is a strong asymmetry of the waves, with wave crests more pronounced than the wave troughs, whereas Eq. (19) assumes a perfect symmetry of the envelopes. A proper model should include the joint probability of the wave crest envelope and wave trough envelope as separate processes that evolve with a lower degree of correlation than that in the case of symmetry. Hence, the joint probability density function of two successive wave heights is expected to take values smaller than the theoretical values. The temporal variation of the wave heights is faster in comparison with that of envelope amplitude, thus produces a smaller correlation coefficient. Notably, the smaller correlation coefficient is associated with the small fetch in Section S7, where the water wave generation has just started.

The mean length of the total run also deviates from the theoretical predictions. In Fig. 15, the mean length of the total run for $H > H_{1/3}$ is
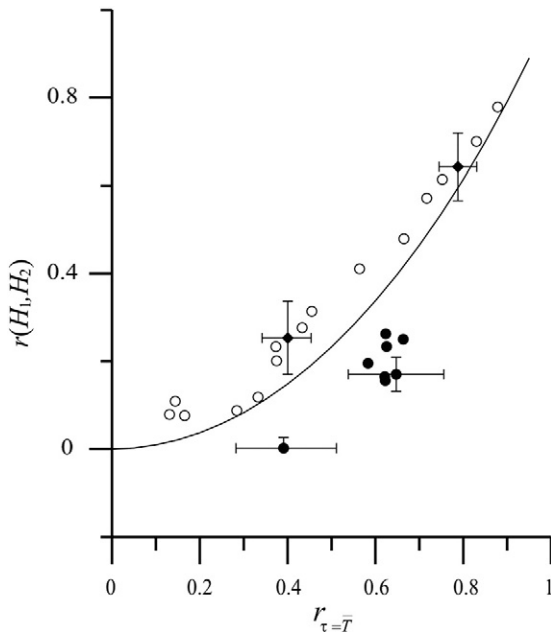
shown, compared with numerical simulations and two field data. The standard deviation of the observation is high, and therefore the quality of agreement is relatively poor. The grouping seems to be present at the early stage of the wave development, but its statistics seem to be slightly different from the statistics for real sea wave data.

3.2. The air flow mean velocity profile

To analyse the air flow boundary layer, the air velocity is acquired at several points in Sections S0–S7, with a space step of 1 mm near the interface and a larger step in the upper region. The data acquisition lasts for 600 s near the free surface with a rate equal to 20 Hz, and for 300 s in the upper region with a rate of 100 Hz.

3.2.1. Measurements over a plain, smooth rigid wall

To check the characteristics of the external flow field and validate the wind tunnel in the modified configuration (with the contraction/expansion elements upstream and downstream of the water tank), the first series of experiments are conducted with the air flow over a plain, smooth PVC wall, rather than the air–water interface. The mean horizontal velocity profiles at eight sections are shown in Fig. 16.

A logarithmic profile is evident in the lower region, and a wake characteristic is expected in the free stream. Curve fitting is carried out based on the "law of wake" proposed by Coles (1956):

$$\frac{U_\infty - U}{u_*} = -\frac{1}{k} \ln \frac{z}{\delta} + \frac{W_c}{k} \left[2 - W\left(\frac{z}{\delta}\right) \right] \qquad (20)$$

where u_* is the friction velocity, U_∞ is the free stream velocity, k is the von Karman constant, δ is the boundary layer thickness, W_c is the wake parameter, and $W(...)$ is the wake function, approximated by (Hinze, 1975).

$$W\left(\frac{z}{\delta}\right) = 1 - \cos\frac{\pi z}{\delta}. \qquad (21)$$

Fig. 14. Relationship between the correlation coefficient and the envelope correlation parameter. Bold line: theory; ○: numerical simulations (Goda, 2000); ◆: field data (Goda, 2000); ●: present experiments, Sections S0–S7, $U_\infty = 10.90$ m/s.
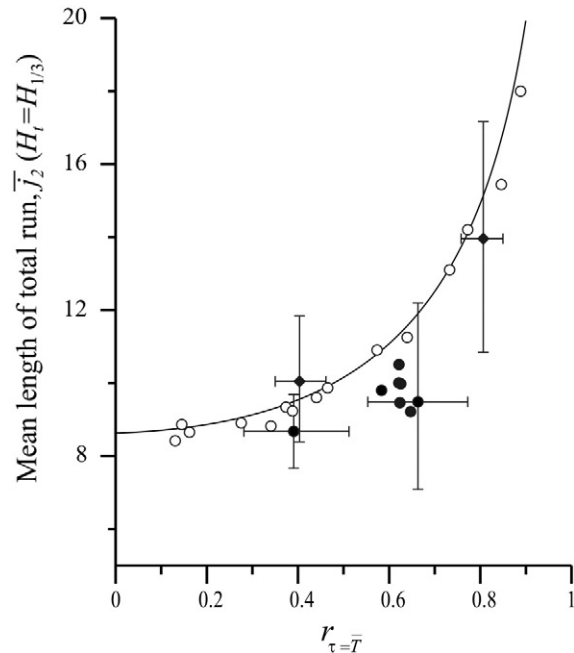
Fig. 15. Comparison of the theoretical and observed results for the mean length of the total run for $H_t = H_{1/3}$. Bold line: theory; ○: numerical simulations (Goda, 2000); ◆: field data (Goda, 2000); ●: present experiments, Sections S0–S7, $U_\infty = 10.90$ m/s.
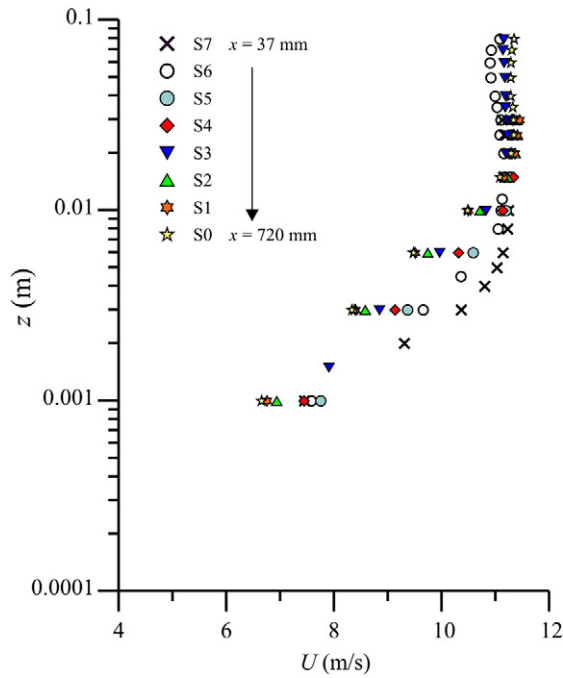
Fig. 16. The horizontal mean wind velocity profiles over a plain, smooth rigid wall. The wind speed in the free stream is $U_\infty = 11.30$ m/s.

The Eq. (20) can also be written as:

$$U^+ = \frac{1}{k}\ln z^+ + C + \frac{W_c}{k}\left[1 - \cos\left(\frac{\pi z^+}{\delta^+}\right)\right] \tag{22}$$

where $U^+ = U/u_*, \delta^+ = \delta u_*/\nu_{air}, z^+ = z u_*/\nu_{air}$, and the constant C is equal to:

$$C = U_\infty^+ - \frac{1}{k}\ln\delta^+ - 2\frac{W_c}{k} \tag{23}$$

where $U_\infty^+ = U_\infty/u_*$.

All the fitted curves achieve a level of confidence greater than 0.95. The values of parameters are presented in Table 4.

The overall behaviour of the boundary-layer is shown in Fig. 17; the velocity gradient in the vertical is shown to be a function of the fetch and the distance normal to the wall.

The entrance geometry influences the structure of the flow at small fetches, but a regular boundary-layer development is observed further downstream. Although not shown here, the kinetic turbulent energy, the Reynolds shear stress and other variables of the process also experience similar trend.

3.2.2. Measurements over water tank

A second series of measurements are about the air flow over water in Sections S0–S7. A finer resolution of the measurements is adopted, and the fan speed is identical to that in the previous section. However, the free stream wind velocity is lower in the presence of water, because of the higher energy loss in the presence of water waves and the presence of the stainless steel wool used to reduce water wave reflection. The mean horizontal velocity profiles are shown in Fig. 18.

For this set of measurements, a logarithmic profile is also evident in the lower region, with a small deviation from the rigid wall boundary layer near the water boundary and in the free stream. The water surface is not at rest (like the rigid wall) but moves, therefore the fitting curve function is:

$$\frac{U_\infty + U_s - U}{u_*} = -\frac{1}{k}\ln\frac{z}{\delta} + \frac{W_c}{k}\left[2 - W\left(\frac{z}{\delta}\right)\right] \tag{24}$$

where U_s is the surface drift. The surface drift is not measured, but estimated by $U_s = 0.55\,u_*$ (Wu, 1975). Eq. (24) can be written in a form similar to the expression (22): $U^+ = (U - U_s)/u_* \equiv U/u_* - 0.55$.

All the fitted curves achieve a confidence level greater than 0.95. The final values are presented in Table 5.

Table 5 also includes the theoretic thickness of the boundary layer, which has been evaluated by using the classical formula (Schlichting and Gersten, 2000):

$$\delta_{teor-lam} = 5\sqrt{\frac{\nu_{air}x}{U_\infty}}\,\text{for}\,\text{Re}_x < 3\cdot10^5 \tag{25}$$

in laminar condition, and

$$\frac{\delta_{teor-turb}U_\infty}{\nu_{air}} = 0.14\frac{\text{Re}_x}{\ln\text{Re}_x}G(\ln\text{Re}_x)\,\text{for}\,\text{Re}_x > 3\cdot10^5 \tag{26}$$

in turbulent condition, with the function G varies weakly with the Reynolds number: 1.5 for $10^5 < \text{Re}_x < 10^6$ and 1 for $\ln\text{Re}_x \to \infty$. The transition strongly depends on background disturbances. The computed friction velocity, except for Sections S7 and S6 where the effects of the entrance geometry are still evident on the structure of the boundary layer, can be predicted by the empirical formula given by Hidy and Plate (1966):

$$u_* = 0.0185\cdot U_\infty^{3/2} \tag{27}$$

where both velocities are in metres per second.

3.2.3. The characteristics of the velocity profiles

The normalised profiles in the wall coordinates for both series of tests are shown in Fig. 19. For small fetches ($x < 220$ mm), the flow needs to adapt to the sudden change of wall geometry, a negative gradient pressure is active which reduces the friction velocity and the flow is generally in a super-smooth regime. A similar behaviour is also
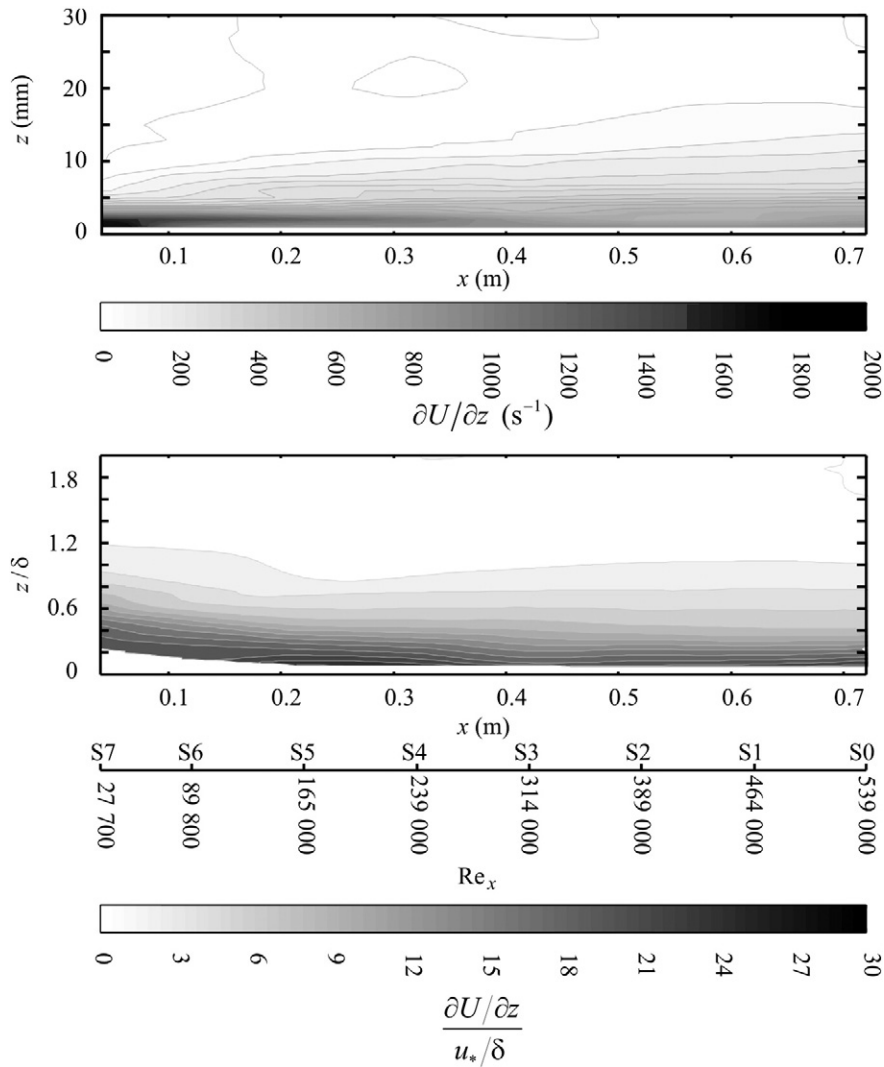
Table 4
Parameters for the mean velocity profiles at different fetches. Measurements in the air over a plain, smooth solid wall. x is the fetch length, U_∞ is the asymptotic velocity, u_* is the friction velocity, δ is the computed thickness of the boundary layer, W_c is the wake coefficient, Re_x is the Reynolds number base on x and on U_∞, and C is the constant in the non-dimensional velocity profile.

Section #	S7	S6	S5	S4	S3	S2	S1	S0
x (mm)	37	120	220	320	420	520	620	720
U_∞ (m/s)	11.30	11.30	11.30	11.30	11.30	11.30	11.30	11.30
u_* (m/s)	0.35	0.35	0.39	0.43	0.44	0.52	0.54	0.53
δ (mm)	4.2	7.2	12.7	13.0	13.8	14.4	15.6	15.7
W_c	1.630	0.847	0.389	0.378	0.417	0.309	0.282	0.324
Re_x ($\times10^5$)	0.277	0.898	1.65	2.39	3.14	3.89	4.64	5.39
C	3.74	3.53	4.53	8.73	9.27	12.39	15.05	12.79

Fig. 17. Velocity gradient in the boundary layer over a plain, smooth rigid wall. In the upper panel, the variables are dimensional and the grey scale is the gradient velocity in s^{-1}; in the lower panel, the variables are non-dimensional with respect to the internal scales of the boundary layer, i.e. the friction velocity u_* and the thickness δ. In addition to the fetch, the axis of the Reynolds number Re_x referred to the distance from the origin is added, with values from 27,700 in Section S7 to 539,000 in Section S0. For a stable well developed boundary layer, the isolines of the non-dimensional velocity gradient plot should be parallel to the bottom. The average wind speed in the free stream is $U_\infty = 11.30$ m/s.

observed on the water side of the flow. For fetch $x > 220$ mm, the profiles almost collapse to the typical profile for turbulent rough flow. Also, the wake parameter W_c decreases sharply when the fetch increases, before retaining a constant value of around 0.35, similar to the value obtained by Hsu et al.(1981).

Some indications can be given about the role of the water waves in determining the nature of the mean flow. Hsu et al. (1981) claimed that, at least for mechanically generated waves by air flow at low wind speed ($U_\infty = 2.4$ m/s), the wave-following properties of the mean profiles should be related to the ripples superposed on the generated wave. This claim is in contrast to that of Stewart (1970), who measured the velocity over flat water and over water waves (similar to those studied in Hsu et al., 1981) but concluded that the waves themselves contributed to roughness, i.e., 'the velocity profile over water waves is quantitatively similar to the profile over a rough plate'. As a consequence, while Hsu et al. (1981) found $C = 8.62$, Stewart found $C = 3.7$ (he found $C = 7.2$ for a smooth flat water surface). According to Hsu et al. (1981), Stewart was wrong in considering the generated water waves as surface roughness: if it were true the coefficient C should decrease for an increasing wind speed keeping constant the wave amplitude, because the relative roughness $a^+ = au_*/\nu$, where a is the wave amplitude, increases due to the increment of the friction velocity. Hence, the reduced value of C was

simply due to the fixed reference chosen by Stewart. In addition, Hsu et al. (1981) claimed that the super-smooth flow coefficient of their experiments (and of Stewart's experiment over a smooth, flat water surface) was a consequence of the surface drift current, which reduced the shear stress and thus C ($C = 5.0$ according to Hussain and Reynolds, 1970, and $C = 6.2$ according to Coles, 1956). In the present experiments, the surface drift velocity effect is included in the computation of the mean velocity profile. As shown in Table 5, the transition between the smooth flow and rough flow is accompanied by a sudden increase in the relative roughness (from 60 in Section 6 to 169 in Section 5). Note that the transition occurs between two sections where the waves are not dramatically different. Therefore, the choice of the reference system should affect the value of C in a similar way. The computed values of C in the two sections are very different ($C = 7.76$ and $C = -3.94$), at least in the present experimental conditions (strong wind and wind-generated waves in limited fetches), so the fixed reference system seems to be adequate for interpreting the mean flow profile with a roughness related to the wave amplitude.

Another frequently used expression for the velocity profile is $\frac{U}{u_*} = \frac{1}{k} \ln \frac{z}{z_0}$ where z_0 is the equivalent surface roughness. The relation between z_0 and the friction/velocity is often parametrized by the Charnock (1955) parameter $\alpha_{Ch} = z_0 g/u_*^2$ which assumes a commonly
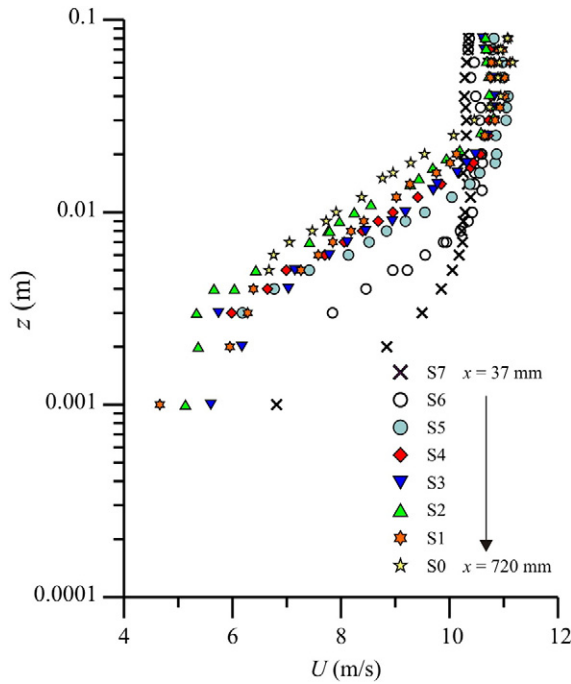
Fig. 18. The horizontal mean wind velocity profiles over water gravity waves in the test sections. The average wind speed in the free stream is $U_\infty = 10.90$ m/s.
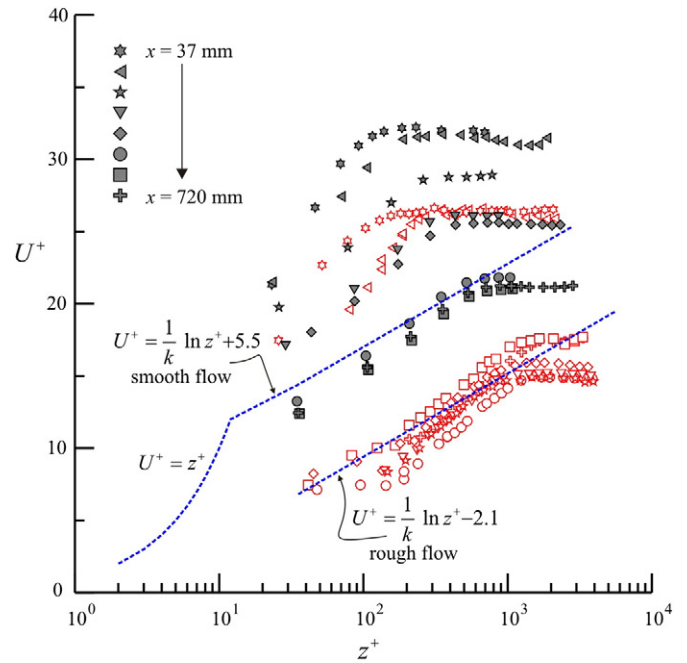

Fig. 19. Normalised profiles of mean streamwise velocity in the wall coordinates at different fetches. Open symbols: flow over water surface. Solid symbols: flow over solid wall.

accepted value equal to 0.0144. The computed Charnock parameter α_{Ch} are reported in Table 5. These values are roughly one order of magnitude smaller than the reference value 0.0144 but well compare with similar results obtained by Liberzon and Shemer (2011) in similar conditions. The authors, for the minimum fetch of their experiments (fetch = 1000 mm) and for wind velocity $U_{10} = 8.6$–13.04 m/s calculate a value $\alpha_{Ch} \sim 0.001$ (see Fig. 5 in Liberzon and Shemer, 2011), while for increasing fetches calculate values which approach the commonly accepted value.

3.2.4. The friction coefficient

The friction coefficient C_f defined by

$$C_f = \frac{\tau_s}{\rho_{air} U_\infty^2} = \left(\frac{u_*}{U_\infty}\right)^2 \tag{28}$$

is plotted against the Reynolds number based on the fetch $\mathrm{Re}_x = U_\infty x / \nu_{air}$ in Fig. 20. The drag of the solid wall reaches the turbulent smooth flow conditions only in the last three sections of measurements

for $\mathrm{Re}_x > 3 \cdot 10^5$, while it is in transition and even in super-laminar flow conditions near the entry section. A similar behaviour is observed for the surface drag on the air–water interface at low Reynolds numbers ($\mathrm{Re}_x < 2 \cdot 10^5$), with a friction coefficient lower than that of a smooth flat plate in the turbulent regime ($C_f = 0.0295 \cdot \mathrm{Re}_x^{-1/5}$) and in the super-laminar condition near the entry section (for laminar flow $C_f = 0.332 \cdot \mathrm{Re}_x^{-1/2}$). However, the transition is very fast, and the friction factor grows, reaching the fully turbulent rough flow value (which satisfied the equation $1.458\left(2C_f\right)^{-2/5} - \ln\sqrt{C_f} = \ln\mathrm{Re}_x$ computed using the experimental equation $C_f = 0.5[2.87 + 0.686 \ln(x/k_s)]^{-5/2}$, where k_s is the roughness height, and assuming the fully turbulent rough flow beyond $k_s u_* / \nu = 70$). In Fig. 20, the results from Hsu and Hsu (1983) are also shown, which are generally in a super-smooth flow regime except for the larger Reynolds number. With sufficient perturbation, the laminar–turbulent transition of the plane boundary layer is reached at $\mathrm{Re}_{xcrit} = 3 \cdot 10^5$, whereas a particularly smooth flow is reached for $\mathrm{Re}_{xcrit} = 3 \cdot 10^6$. For the present tests over a rigid plane, the transition starts at $\mathrm{Re}_{xcrit} \sim 10^5$. This point is further discussed in the following analysis of the boundary layer thickness. In general, the

Table 5

Parameters for mean velocity profiles at different fetches. Measurements in air over water. x is the fetch length, U_∞ is the asymptotic velocity, u_* is the friction velocity, δ is the computed thickness of the boundary layer, W_c is the wake coefficient, Re_x is the Reynolds number based on x and on U_∞, C is the constant in the non-dimensional velocity profile, $\delta_{teor\text{-}tur}$ and $\delta_{teor\text{-}lam}$ are the theoretical boundary layer thicknesses in turbulent and laminar condition, $a_{c\text{-}rms}$ is the root mean square amplitude of the crest, a^+ is the non-dimensional roughness based on $a_{c\text{-}rms}$, and α_{Ch} is the Charnock parameter.

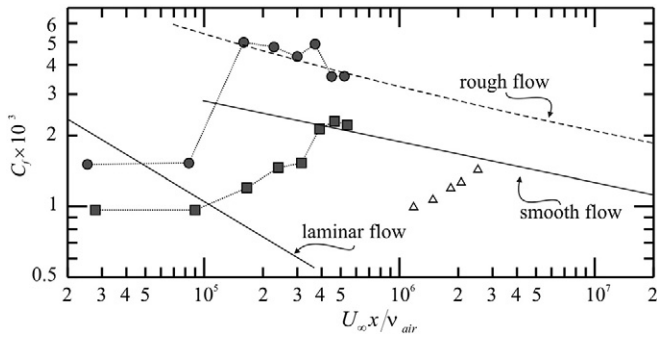| Section #	S7	S6	S5	S4	S3	S2	S1	S0
x (mm)	37	120	220	320	420	520	620	720
U_∞ (m/s)	10.30	10.50	10.93	10.72	10.74	10.72	10.94	10.92
u_* (m/s)	0.39	0.40	0.74	0.71	0.68	0.72	0.63	0.63
δ (mm)	3.9	9.4	18.0	19.1	21.2	24.6	28.0	36.2
W_c	1.209	0.939	0.350	0.375	0.322	0.323	0.348	0.412
Re_x (×10^5)	0.252	0.834	1.59	2.27	2.99	3.69	4.49	5.21
C	8.84	7.76	−3.94	−3.78	−2.97	−4.39	−1.90	−2.95
$\delta_{teor\text{-}turb}$ (mm)	1.4	2.2	3.9	5.4	7.0	8.5	10.0	11.5
$\delta_{teor\text{-}lam}$ (mm)	0.4	0.6	0.8	0.8	0.9	0.9	1.0	1.1
$a_{c\text{-}rms}$ (mm)	1.31	2.26	3.44	3.56	3.3	3.17	3.18	3.29
a^+	34	60	169	167	149	151	133	137
α_{Ch}	0.0034	0.0023	0.0037	0.0025	0.0028	0.0028	0.0013	0.0007

Fig. 20. Wind-friction coefficient C_f as a function of the Reynolds number. $\triangle$ Hsu and Hsu (1983); $\bullet$, this experiment, air flow over water; $\blacksquare$, this experiment, air flow over a planar smooth rigid wall.

wall roughness encourages the laminar–turbulent transition because the roughness produces additional disturbances and reduces the critical Reynolds number, but there are very few measurement of this transition over a rough surface. The critical Reynolds number drops only if the non-dimensional roughness height $U_\infty k_s/\nu > 120$ (Schlichting and Gersten, 2000). For the present experiments, a roughness height of $k_s > 0.16$ mm was sufficient for the transition. Assuming $k_s \propto H_{rms}$, it results in an earlier transition in the presence of water waves with respect to a smooth flat plate.

3.2.5. The thickness of the boundary layer

A good indicator of the boundary layer evolution is its streamwise thickness variation. The developments of the measured and theoretical boundary-layer thickness are compared in Fig. 21.

The laminar and turbulent relationships refer to the boundary layer developed on a flat plate. In fact, the ramp of the water tank in this experiments accelerates the boundary layer, which is already turbulent but confined; then, beyond the junction section between the upstream ramp and the horizontal rigid plane (or the wave tank), limited growth is observed the boundary layer thickness. Due to the spatial evolution of the boundary, a progressive adaptation of the boundary layer occurs. 500 mm is added to the theoretical turbulent boundary layer thickness to fit the evolution measured on a rigid plane
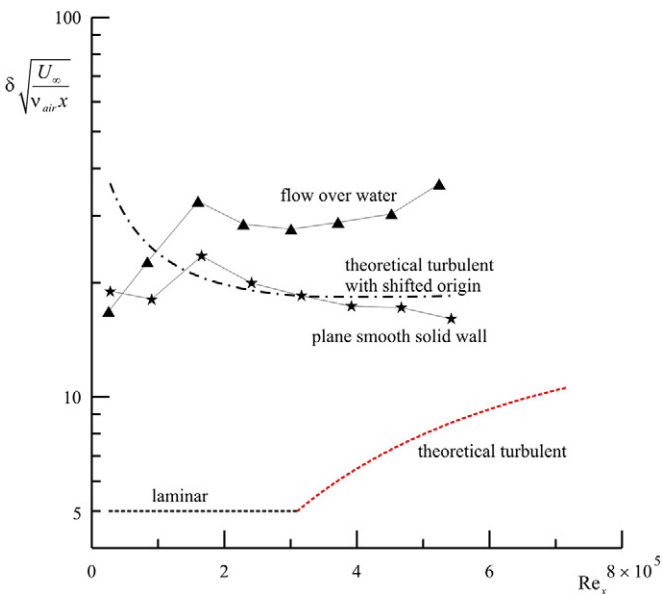
bottom, obtaining the dot-dashed curve in Fig. 22. Further deviations from the theoretic profile are attributed to the effect of displacement, i.e., the interaction with the outer flow, which slightly modifies the asymptotic free stream velocity.

As seen in Fig. 22, the boundary layer thickness increases with fetch monotonically, but the growth rate is much higher for the boundary layer over waves. For both experimental profiles (over a solid wall and over water), a sudden change in the boundary-layer thickness growth is evident at a fetch of 200 mm. Close to this fetch, the re-adaptation process of the boundary layer has almost completed.

4. Conclusions

A series of experiments was planned in a wind tunnel with a water tank in order to analyse the efficiency in momentum transfer from the wind to gravity waves. Gravity waves are generated entirely by the wind. Several parameters of the wind flow field and of the gravity waves are experimentally evaluated and compared with existing theories or other experiments. Amongst them the friction coefficient and the velocity drift at the surface of the water are analysed in details. The aim of the experiments is a deeper analysis of the phenomena occurring, in nature, at different scales, controlling the energy budget on a planetary scale and wave growth, wave breaking, meteorological tides at smaller scales.

- The wind-generated waves show the typical growing trend with fetch and wind speed and are also asymmetric, with crests more pronounced than troughs.
- The phase and group velocities of the waves are computed using a cross-correlation technique of the water level measured in several spaced sections. The phase velocity, due to the current in the tank flowing in the direction of wave propagation, as expected, is larger than the theoretical velocity in the absence of the current and is affected by wind drift and Stokes current, which are variable in space. The group velocity is affected in a similar way, and a model is developed to account for the relative variation of phase velocity and group velocity, which includes a dependence of the drift velocity from the wave steepness.
- The wave grouping is detected, with a statistic of the runs and of the total runs close to the statistic measured for real sea waves. The
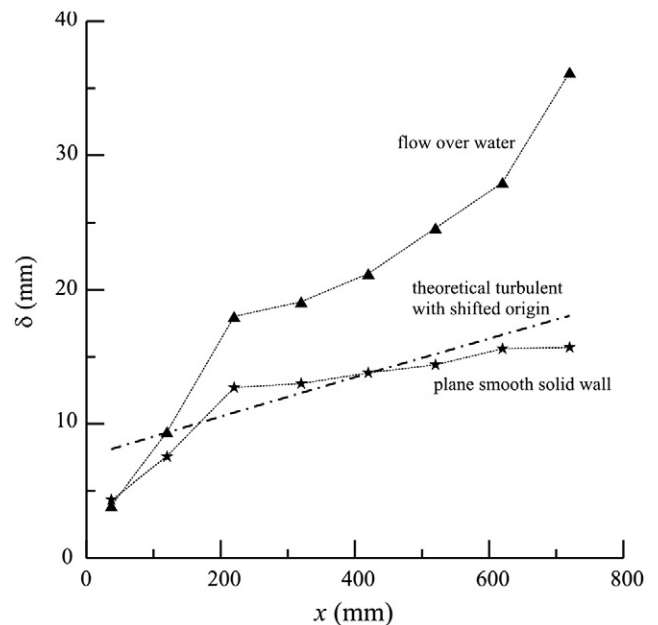

Fig. 21. Dependence of the boundary-layer thickness on the Reynolds number. The turbulent boundary layer equation was represented with a fictitious origin at $\mathrm{Re}_x = 1.5 \cdot 10^5$ to have the transition at $\mathrm{Re}_x = 3 \cdot 10^5$. The dot-dashed line fits the turbulent profile to reproduce the measured profile on a rigid bottom.

Fig. 22. Evolution of the boundary-layer thickness with the fetch.

correlation coefficient between two successive wave heights is generally smaller than the theoretical coefficient because of the asymmetry of the waves, which suggests that the envelope of the crests and the envelope of the troughs should be treated separately.

- The air flow boundary layer over the water waves shows a logarithmic profile with a wake near the free stream. The apparent roughness is related to the wave amplitude, and the flow is turbulent with the friction coefficient typical of a full rough flow, except for sections with limited fetch. The transition to turbulence occurs at an earlier stage with respect to the transition of a boundary layer over a smooth, flat rigid wall. The thickness of the boundary layer over the water waves grows much faster than for the boundary layer over a plain, smooth solid wall.

Acknowledgements

References

Banner, M.L., Peregrine, D.H., 1993. Wave breaking in deep water. Annual Review of Fluid Mechanics 25, 373–397.
Bendat, G.S., Piersol, A.G., 2000. Random Data Analysis and Measurement Procedures. Wiley & Sons, New York.
Brocchini, M., Peregrine, D.H., 2001. The dynamics of strong turbulence at free surfaces. Part 1. Description. Journal of Fluid Mechanics 449, 225–254.
Caulliez, G., Ricci, N., Dupont, R., 1998. The generation of the first visible wind waves. Physics Fluids Letters 10 (4), 757–759.
Cavaleri, L., Zecchetto, S., 1987. Reynolds stresses under wind waves. Journal of Geophysical Research C4, 3894–3904.
Charnock, H., 1955. Wind stress on water surface. Quarterly Journal of the Royal Meteorological Society 81, 639–640.
Chiapponi, L., Longo, S., Bramato, S., Mans, C., Losada, M.A., 2011. Waves generated by wind. Experiments carried out in wind tunnel II. Technical Report. CEAMA, Granada, Spain.
Coles, D.W., 1956. The law of the wake in the turbulent boundary layer. Journal of Fluid Mechanics 1, 191–226.
Gerbi G P (2008) Observations of turbulent fluxes and turbulence dynamics in the ocean surface boundary layer. Ph.D. thesis, Woods Hole Oceanographic Institution-Massachusetts Institute of Technology, Woods Hole, MA, 119 pp
Goda, Y., 2000. Random Seas and Design of Maritime Structures. World Scientific Publishing, Singapore.
Hinze, J.O., 1975. Turbulence. McGraw-Hill.
Hsu, C.-T., Hsu, E.-Y., Street, R.L., 1981. On the structure of turbulent flow over a progressive water wave: theory and experiment in a transformed, wave-following coordinate system. Journal of Fluid Mechanics 105, 87–117.
Hsu, C.-T., Hsu, E.-Y., 1983. On the structure of turbulent flow over a progressive water wave: theory and experiment in a transformed, wave-following coordinate system. Part 2. Journal of Fluid Mechanics 131, 123–153.
Hidy, G.M., Plate, E.J., 1966. Wind action on water standing in a laboratory channel. Journal of Fluid Mechanics 26, 651–687.
Hussain, A.K.M.F., Reynolds, W.C., 1970. The mechanics of an organized wave in turbulent shear flow. Journal of Fluid Mechanics 41, 241–258.
Jacobs, S.J., Gwinn, A.W., 1999. Doppler shifting of water waves by a turbulent wind-driven current. Proceedings of the IEEE Sixth Working Conference on Current Measurement, pp. 45–48.

Kawai, S., 1979. Generation of initial wavelets by instability of a coupled shear flow and their evolution to wind waves. Journal of Fluid Mechanics 93, 661–703.
Keulegan, G.H., 1951. Wind tides in small closed channels. Journal of Research of the National Bureau of Standards 46 (5), 358–381.
Kimura, A., 1980. Statistical properties of random wave groups. Proc 17th Int Conf Coastal Engrg, pp. 2955–2973.
Kitaigorodskii, S.A., Donelan, M.A., Lumley, J.L., Terray, E.A., 1983. Wave-turbulence interactions in upper ocean. Part II: statistical characteristics of wave and turbulent components of the random velocity field in the marine surface layer. Journal of Physical Oceanography 13, 1988–1999.
Liberzon, D., Shemer, L., 2011. Experimental study of the initial stages of wind waves' spatial evolution. Journal of Fluid Mechanics 681, 462–498.
Longuet-Higgins, M.S., 1969. Action of a variable stress at the surface of water waves. Physics of Fluids 12, 737–740.
Masch, F.D., 1963. Mixing and dispersive action of wind waves. International Journal of Air and Water Pollution 7, 69.
McKenna S P (2000) Free-surface turbulence and air–water exchange. PhD Thesis, Dep of Applied Ocean Physics, WHOI and Engineering and Department of Ocean Engineering, MIT.
Melville, W.K., Shear, R., Veron, F., 1998. Laboratory measurements of the generation and evolution of Langmuir circulations. Journal of Fluid Mechanics 364, 31–58.
Miles, J.W., 1957. On the generation of surface waves by shear flows. Journal of Fluid Mechanics 3, 185–204.
Perry, A.E., Lim, K.L., Henbest, S.M., 1987. An experimental study of the turbulent structure in smooth- and rough-wall boundary layers. Journal of Fluid Mechanics 177, 437–466.
Plant, W.J., Wright, J.W., 1980. Phase speeds of upwind and downwind traveling short gravity waves. Journal of Geophysical Research 85 (C6), 3304–3310.
Phillips, O.M., 1957. On the generation of waves by turbulent wind. Journal of Fluid Mechanics 2, 417–445.
Rice, S.O., 1944. Mathematical analysis of random noise. Bell System Technical Journal 23, 282–332 Reprinted Selected Papers on Noise and Stochastic Processes (1954), Dover, 132–294.
Rice, S.O., 1945. Mathematical analysis of random noise. Bell System Technical Journal 24, 46–156 Reprinted Selected Papers on Noise and Stochastic Processes (1954), Dover, 132–294.
Schlichting, H., Gersten, K., 2000. Boundary Layer Theory. Springer, Berlin.
Shaikh, N., Siddiqui, K., 2011. Near-surface flow structure over wind-generated water waves, part I: wave-induced flow characteristics. Ocean Dynamics 61, 127–141.
Shaw, W.J., Trowbridge, J.H., 2001. The direct estimation of near-bottom turbulent fluxes in the presence of energetic wave motions. Journal of Atmospheric and Oceanic Technology 18, 1540–1557.
Shen, L., Yue, D.K.P., 2001. Large-eddy simulation of free-surface turbulence. Journal of Fluid Mechanics 440, 75–116.
Siddiqui, M.H.K., Loewen, M.R., 2007. Characteristics of the wind drift layer and microscale breaking waves. Journal of Fluid Mechanics 573, 417–456.
Siddiqui, M.H.K., Loewen, M.R., Asher, W.E., Jessup, A., 2004. Coherent structures beneath wind waves and their influence on air–water gas transfer. Journal of Geophysical Research 109 (C3), C03024.
Stewart, R.H., 1970. Laboratory studies of the velocity field over deep-water waves. Journal of Fluid Mechanics 42, 733–754.
Sullivan, P.P., McWilliams, J.C., 2010. Dynamics of winds and currents coupled to surface waves. Annual Review of Fluid Mechanics 42, 19–42.
Taylor, J.R., 1997. An Introduction to Error Analysis. University Science Books.
Teixeira, M.A.C., Belcher, S.E., 2006. On the initiation of surface waves by turbulent shear flow. Dynamics of Atmospheres and Oceans 41, 1–27.
Trowbridge, J.H., 1998. On a technique for measurement of turbulent shear stress in the presence of surface waves. Journal of Atmospheric and Oceanic Technology 15, 290–298.
Veron, F., Melville, W.K., 2002. Experiments on the stability and transition of wind-driven water surfaces. Journal of Fluid Mechanics 446, 25–65.
Valenzuela, G.R., 1976. The growth of gravity-capillary waves in the coupled shear flow. Journal of Fluid Mechanics 76, 229–250.
van Gastel, K., Janssen, P.A.E.M., Komen, G.J., 1985. On phase velocity and growth rate of wind-induced gravity-capillary waves. Journal of Fluid Mechanics 161, 199–216.
Wu, J., 1975. Wind-induced drift current. Journal of Fluid Mechanics 68, 49–70.